

# Three-dimensional *in vivo* fluorescence diffuse optical tomography of breast cancer in humans

Alper Corlu<sup>1</sup>, Regine Choe<sup>1</sup>, Turgut Durduran<sup>1,2</sup>, Mark A. Rosen<sup>2</sup>,  
Martin Schweiger<sup>3</sup>, Simon R. Arridge<sup>3</sup>, Mitchell D. Schnall<sup>2</sup>,  
Arjun G. Yodh<sup>1</sup>

<sup>3</sup>Department of Computer Science, University College London, Gower Street, London WC1E 6BT, UK

<sup>1</sup>Department of Physics and Astronomy, <sup>2</sup>Department of Radiology, University of Pennsylvania, Philadelphia, Pennsylvania 19104

Phone: 1-215-573-3463, Fax: 1-215-573-6391, [corlua@alumni.upenn.edu](mailto:corlua@alumni.upenn.edu)

<http://www.lrsm.upenn.edu/pmi>, <http://www.physics.upenn.edu/yodhlab/>

**Abstract:** We present three-dimensional (3D) *in vivo* images of human breast cancer based on fluorescence diffuse optical tomography (FDOT). To our knowledge, this work represents the first reported 3D fluorescence tomography of human breast cancer *in vivo*. In our protocol, the fluorophore Indocyanine Green (ICG) is injected intravenously. Fluorescence excitation and detection are accomplished in the soft-compression, parallel-plane, transmission geometry using laser sources at 786 nm and spectrally filtered CCD detection. Phantom and *in vivo* studies confirm the signals are due to ICG fluorescence, rather than tissue autofluorescence and excitation light leakage. Fluorescence images of breast tumors were in good agreement with those of MRI, and with DOT based on endogenous contrast. Tumor-to-normal tissue contrast based on ICG fluorescence was two-to-four-fold higher than contrast based on hemoglobin and scattering parameters. In total the measurements demonstrate that FDOT of breast cancer is feasible and promising.

© 2007 Optical Society of America

**OCIS codes:** (170.6280) Spectroscopy, fluorescence and luminescence; (170.3010) Image reconstruction techniques; (170.3830) Mammography

---

## References and links

1. A. G. Yodh and B. Chance, Spectroscopy and imaging with diffusing light, *Physics Today* 48, 34–40 (1995).
2. A. G. Yodh and D. A. Boas, Biomedical Photonics, chapter Functional Imaging with Diffusing Light, (CRC Press, 2003) pp. 21/1–45.
3. J. P. Culver, R. Choe, M. J. Holboke, L. Zubkov, T. Durduran, A. Slemper, V. Ntziachristos, D. N. Pattanayak, B. Chance, and A. G. Yodh, 3D diffuse optical tomography in the plane parallel transmission geometry: Evaluation of a hybrid frequency domain/continuous wave clinical system for breast imaging, *Med. Phys.* 30, 235–247 (2003).
4. R. Choe, A. Corlu, K. Lee, T. Durduran, S. D. Konecky, M. Grosicka-Koptyra, S. R. Arridge, B. J. Czerniecki, D. L. Fraker, A. DeMichele, B. Chance, M. A. Rosen, and A. G. Yodh, Diffuse optical tomography of breast cancer during neoadjuvant chemotherapy: a case study with comparison to MRI, *Med. Phys.* 32, 1128–1139 (2005).

5. T. Durduran, R. Choe, J. P. Culver, L. Zubkov, M. J. Holboke, J. Giammarco, B. Chance, and A. G. Yodh, Bulk optical properties of healthy female breast tissue, *Phys. Med. Biol.* 47, 2847–2861 (2002).
6. A. E. Cerussi, A. J. Berger, F. Bevilacqua, N. Shah, D. Jakubowski, J. Butler, R. F. Holcombe, and B. J. Tromberg, Sources of absorption and scattering contrast for near-infrared optical mammography, *Acad. Radiol.* 8, 211–218 (2001).
7. T. O. McBride, B. W. Pogue, S. D. Jiang, and U. L. Osterberg, A parallel-detection frequency-domain near-infrared tomography system for hemoglobin imaging of the breast in vivo, *Rev. Sci. Instrum.* 72, 1817–1824 (2001).
8. V. Ntziachristos and B. Chance, Probing physiology and molecular function using optical imaging: applications to breast cancer, *Breast Cancer Res.* 3, 41–46 (2001).
9. B. W. Pogue, S. P. Poplack, T. O. McBride, W. A. Wells, K. S. Osterman, U. L. Osterberg, and K. D. Paulsen, Quantitative hemoglobin tomography with diffuse near-infrared spectroscopy: Pilot results in the breast, *Radiology* 218, 261–266 (2001).
10. N. Shah, A. Cerussi, C. Eker, J. Espinoza, J. Butler, J. Fishkin, R. Hornung, and B. Tromberg, Noninvasive functional optical spectroscopy of human breast tissue, *Proc. Natl. Acad. Sci.* 98, 4420–4425 (2001).
11. A. Garofalakis, G. Zacharakis, G. Filippidis, E. Sanidas, D. D. Tsiftsis, E. Stathopoulos, M. Kafousi, J. Ripoll, and TG Papazoglou, Optical characterization of thin female breast biopsies based on the reduced scattering coefficient, *Phys. Med. Biol.* 50, 2583–2596 (2005).
12. F. Martelli and G. Zaccanti, Calibration of scattering and absorption properties of a liquid diffusive medium at NIR wavelengths. CW method, *Opt. Express* 15, 486–500 (2007).
13. V. Ntziachristos, A. G. Yodh, M. Schnall, and B. Chance, Concurrent MRI and diffuse optical tomography of breast after indocyanine green enhancement, *Proc. Natl. Acad. Sci.* 97, 2767–2772 (2000).
14. X. Intes, J. Ripoll, Y. Chen, S. Nioka, A. G. Yodh, and B. Chance, In vivo continuous-wave optical breast imaging enhanced with indocyanine green, *Med. Phys.* 30, 1039–1047 (2003).
15. R. Weissleder, C. H. Tung, U. Mahmood, and A. Bogdanov, In vivo imaging of tumors with protease-activated near-infrared fluorescent probes, *Nat. Biotechnol.* 17, 375–378 (1999).
16. D. J. Hawrysz and E. M. Sevick-Muraca, Developments Toward Diagnostic Breast Cancer Imaging Using Near-Infrared Optical Measurements and Fluorescent Contrast Agents, *Neoplasia* 2, 388–417 (2000).
17. V. Ntziachristos, C. Tung, C. Bremer, and R. Weissleder, Fluorescence molecular tomography resolves protease activity in vivo, *Nat. Med.* 8, 757–760 (2002).
18. R. Cheung, M. Solonenko, T. M. Busch, F. Del Piero, M. E. Putt, S. M. Hahn, and A. G. Yodh, Correlation of in vivo photosensitizer fluorescence and photodynamic-therapy-induced depth of necrosis in a murine tumor model, *J. Of Biomed. Opt.* 8, 248–252 (2003).
19. S. Ke, X. Wen, M. Gurfinkel, C. Charnsangavej, S. Wallace, E. M. Sevick-Muraca, and C. Li, Near-infrared optical imaging of epidermal growth factor receptor in breast cancer xenografts, *Cancer Res.* 63, 7870–7875 (2003).
20. A. Bogaards, A. Varma, K. Zhang, D. Zach, S. K. Bisland, E. H. Moriyama, L. Lilge, P. J. Muller, and B. C. Wilson, Fluorescence image-guided brain tumour resection with adjuvant metronomic photodynamic therapy: pre-clinical model and technology development, *Photochem. Photobiol. Sci.* 4, 438–442 (2005).
21. T. H. Foster, B. D. Pearson, S. Mitra, and C. E. Bigelow, Fluorescence anisotropy imaging reveals localization of meso-tetrahydroxyphenyl chlorin in the nuclear envelope, *Photochem. Photobiol.* 81, 1544–1547 (2005).
22. P. I. Bastiaens and A. Squire, Fluorescence lifetime imaging microscopy: spatial resolution of biochemical processes in the cell, *Trends Cell Biol.* 9, 48–52 (1999).
23. E. Kuwana and E. M. Sevick-Muraca, Fluorescence lifetime spectroscopy for pH sensing in scattering media, *Anal. Chem.* 75, 4325–4329 (2003).
24. E. Bombardieri and F. Crippa, PET imaging in breast cancer, *Q. J. of Nucl. Med.* 45, 245–55 (2001).
25. A. R. Padhani, Dynamic contrast-enhanced MRI in clinical oncology: current status and future directions, *J. Magn. Reson. Imaging* 16, 407–422 (2002).
26. B. Ballou, G. W. Fisher, A. S. Waggoner, D. L. Farkas, J. M. Reiland, R. Jaffe, R. B. Mujumdar, S. R. Mujumdar, and T. R. Hakala, Tumor labeling in vivo using cyanine-conjugated monoclonal antibodies, *Cancer Immunol. Immunother.* 41, 257–263 (1995).
27. S. Achilefu, R. B. Dorshow, J. E. Bugaj, and R. Rajagopalan, Novel receptor-targeted fluorescent contrast agents for in vivo tumor imaging, *Invest. Radiol.* 35, 479–485 (2000).
28. U. Mahmood, C.H. Tung, Y. Tang, and R. Weissleder, Feasibility of in Vivo Multichannel Optical Imaging of Gene Expression: Experimental Study in Mice1 (2002).
29. S. Kwon, S. Ke, J. P. Houston, W. Wang, Q. Wu, C. Li, and E. M. Sevick-Muraca, Imaging dose-dependent pharmacokinetics of an RGD-fluorescent dye conjugate targeted to alpha v beta 3 receptor expressed in Kaposi's sarcoma, *Mol. Imaging* 4, 75–87 (2005).
30. A. Tsourkas and G. Bao, Shedding light on health and disease using molecular beacons. *Brief Funct. Genomic. Proteomic.* 1, 372–384 (2003).
31. M. A. O'Leary, D. A. Boas, B. Chance, and A. G. Yodh, Retardation and imaging of diffuse photon density waves using fluorescent inhomogeneities. *J. Lumin.* 60-1, 281–286 (1994).

32. M. A. O'Leary, D. A. Boas, X. D. Li, B. Chance, and A. G. Yodh, Fluorescent lifetime imaging in turbid media. *Opt. Lett.* 21, 158–160 (1996).
33. J. Wu, L. Perelman, R. R. Dasari, and M. S. Feld, Fluorescence tomographic imaging in turbid media using early-arriving photons and Laplacetransforms. *Proc. Natl. Acad. Sci.* 94, 8783–8788 (1997).
34. B. B. Das, F. Liu, and R. R. Alfano, Time-resolved fluorescence and photon migration studies in biomedical and model random media. *Rep. Prog. Phys.* 60, 227–292 (1997).
35. X. D. Li, B. Chance, and A. G. Yodh, Fluorescent heterogeneities in turbid media: limits for detection, characterization, and comparison with absorption, *Applied Optics* 37, 6833–6844 (1998).
36. E. L. Hull, M. G. Nichols, and T. H. Foster, Localization of luminescent inhomogeneities in turbid media with spatially resolved measurements of cw diffuse luminescence emittance, *Appl. Opt.* 37, 2755–2765 (1998).
37. M. J. Eppstein, D. J. Hawrysz, A. Godavarty, and E. M. Sevick-Muraca, Three-dimensional, Bayesian image reconstruction from sparse and noisy data sets: Near-infrared fluorescence tomography, *Proc. Natl. Acad. Sci.* 99, 9619–9624 (2002).
38. A. D. Klose and A. H. Hielscher, Fluorescence tomography with simulated data based on the equation of radiative transfer, *Opt. Lett.* 28, 1019–1021 (2003).
39. V. Ntziachristos and R. Weissleder, CCD-based scanner for three-dimensional fluorescence-mediated diffuse optical tomography of small animals, *Med. Phys.* 29, 803–809 (2002).
40. E. Shives, Y. Xu, and H. Jiang, Fluorescence lifetime tomography of turbid media based on an oxygen-sensitive dye, *Opt. Express* 10, 1557–1562 (2002).
41. Y. Chen, C. Mu, X. Intes, D. Blessington, and B. Chance, Near-infrared phase cancellation instrument for fast and accurate localization of fluorescent heterogeneity, *Rev. Sci. Instrum.* 74, 3466–3473 (2003).
42. K. R. Diamond, T. J. Farrell, and M. S. Patterson, Measurement of fluorophore concentrations and fluorescence quantum yield in tissue-simulating phantoms using three diffusion models of steady-state spatially resolved fluorescence, *Phys. Med. Biol.* 48, 4135–4149 (2003).
43. S. C. Davis, B. W. Pogue, H. Dehghani, and K. D. Paulsen, Contrast-detail analysis characterizing diffuse optical fluorescence tomography image reconstruction, *J. Biomed. Opt.* 10, 050501–050501 (2005).
44. A. T. N. Kumar, S. B. Raymond, G. Boverman, D. A. Boas, and B. J. Bacskai, Time resolved fluorescence tomography of turbid media based on lifetime contrast, *Opt. Express* 14, 12255–12270 (2006).
45. A. Joshi, W. Bangerth, K. Hwang, J. C. Rasmussen, and E. M. Sevick-Muraca, Fully adaptive FEM based fluorescence optical tomography from time-dependent measurements with area illumination and detection, *Med. Phys.* 33, 1299–1310 (2006).
46. A. Godavarty, A. B. Thompson, R. Roy, M. Gurfinkel, M. J. Eppstein, C. Zhang, and E. M. Sevick-Muraca, Diagnostic imaging of breast cancer using fluorescence-enhanced optical tomography: phantom studies, *J. Biomed. Opt.* 9, 488–496 (2004).
47. D. E. Hyde, T. J. Farrell, M. S. Patterson, and B. C. Wilson, A diffusion theory model of spatially resolved fluorescence from depth-dependent fluorophore concentrations, *Phys. Med. Biol.* 46, 369–383 (2001).
48. S. V. Apreleva, D. F. Wilson, and S. A. Vinogradov, Tomographic imaging of oxygen by phosphorescence lifetime, *Appl. Opt.* 45, 8547–8559 (2006).
49. S. Li, Q. Zhang, and H. Jiang, Two-dimensional bioluminescence tomography: numerical simulations and phantom experiments, *Appl. Opt.* 45, 3390–3394 (2006).
50. H. Dehghani, S. C. Davis, S. Jiang, B. W. Pogue, K. D. Paulsen, and M. S. Patterson, Spectrally resolved bioluminescence optical tomography, *Opt. Lett.* 31, 365–367 (2006).
51. E. E. Graves, J. Ripoll, R. Weissleder, and V. Ntziachristos, A submillimeter resolution fluorescence molecular imaging system for small animal imaging, *Med. Phys.* 30, 901 (2003).
52. B. W. Pogue, S. L. Gibbs, B. Chen, and M. Savellano, Fluorescence imaging in vivo: raster scanned point-source imaging provides more accurate quantification than broad beam geometries, *Technol. Cancer Res. Treat.* 3, 15–21 (2004).
53. S. V. Patwardhan, S. R. Bloch, S. Achilefu, and J. P. Culver, Time-dependent whole-body fluorescence tomography of probe bio-distributions in mice, *Opt. Express* 13, 2564–2577 (2005).
54. K. Hwang, J. P. Houston, J. C. Rasmussen, A. Joshi, S. Ke, C. Li, and E. M. Sevick-Muraca, Improved excitation light rejection enhances small-animal fluorescent optical imaging, *Mol. Imaging* 4, 194–204 (2005).
55. S. Bloch, F. Lesage, L. McIntosh, A. Gandjbakhche, K. Liang, and S. Achilefu, Whole-body fluorescence lifetime imaging of a tumor-targeted near-infrared molecular probe in mice. *J. of Biomed. Opt.* 10, 54003–54003 (2005).
56. A. Liebert, H. Wabnitz, J. Steinbrink, M. Moller, R. Macdonald, H. Rinneberg, A. Villringer, and H. Obrig, Bed-side assessment of cerebral perfusion in stroke patients based on optical monitoring of a dye bolus by time-resolved diffuse reflectance, *Neuroimage* 24, 426–35 (2005).
57. J. S. Reynolds, T. L. Troy, R. H. Mayer, A. B. Thompson, D. J. Waters, K. K. Cornell, P. W. Snyder, and E. M. Sevick-Muraca, Imaging of spontaneous canine mammary tumors using fluorescent contrast agents, *Photochem. Photobiol.* 70, 87–94 (1999).
58. Akorn Inc. IC-GREEN<sup>TM</sup>. [http://www.akorn.com/documents/catalog/package\\_inserts/17478-701-02.pdf](http://www.akorn.com/documents/catalog/package_inserts/17478-701-02.pdf), 2005. Accessed 2/13/07.
59. S. R. Arridge, Optical tomography in medical imaging, *Inverse Problems* 15, R41–R93 (1999).

60. M. A. O'Leary, *Imaging with diffuse photon density waves*, Ph.D. Dissertation University of Pennsylvania, 1996.
61. S. R. Arridge and M. Schweiger, A gradient-based optimisation scheme for optical tomography, *Opt. Express* 2, 213–226 (1998).
62. A. Corlu, R. Choe, T. Durduran, K. Lee, M. Schweiger, E. M. C. Hillman, S. R. Arridge, and A. G. Yodh, Diffuse optical tomography with spectral constraints and wavelength optimization, *Appl. Opt.* 44, 2082–2093 (2005).
63. A. Corlu, T. Durduran, R. Choe, M. Schweiger, E. M. C. Hillman, S. R. Arridge, and A. G. Yodh, Uniqueness and wavelength optimization in continuous-wave multispectral diffuse optical tomography, *Opt. Lett.* 28, 2339–2341 (2003).
64. D. A. Boas, *Diffuse Photon Probes of Structural and Dynamical Properties of Turbid Media: Theory and Biomedical Applications*, Ph.d. dissertation, University of Pennsylvania, 1996.
65. T. Durduran, A. G. Yodh, B. Chance, and D. A. Boas, Does the photon diffusion coefficient depend on absorption? *J. Opt. Soc. Am.* 14, 3358–3365 (1997).
66. D. J. Durian, The diffusion coefficient depends on absorption, *Opt. Lett.* 23, 1502–1504 (1998).
67. M. Schweiger, S. R. Arridge, M. Hiraoka, and D. T. Delpy, The finite element model for the propagation of light in scattering media: Boundary and source conditions, *Med. Phys.* 22, 1779–1792 (1995).
68. V. Ntziachristos and R. Weissleder, Experimental three-dimensional fluorescence reconstruction of diffuse media by use of a normalized Born approximation, *Opt. Lett.* 26, 893–895 (2001).
69. M. Schweiger, S. R. Arridge, and I. Nissilä, Gauss-Newton method for image reconstruction in diffuse optical tomography, *Phys. Med. Biol.* 50, 2365–2386 (2005).
70. H. W. Engl, M. Hanke, and A. Neubauer, *Regularization of Inverse Problems* (Kluwer Academic Publishers, 1996).
71. S. R. Arridge, M. Schweiger, M. Hiraoka, and D. T. Delpy, A finite element approach for modeling photon transport in tissue, *Med. Phys.* 20, 299–309 (1993).
72. S. Prahl, Optical properties spectra, <http://omlc.org/spectra/index.html>, 2001. Accessed 2/14/07.
73. E. M. Sevick-Muraca, G. Lopez, J. S. Reynolds, T. L. Troy, and C. L. Hutchinson, Fluorescence and absorption contrast mechanisms for biomedical optical imaging using frequency-domain techniques, *Photochem. Photobiol.* 66, 55–64 (1997).
74. H. Dehghani, B. W. Pogue, S. P. Poplack, and K. D. Paulsen, Multiwavelength three-dimensional near-infrared tomography of the breast: initial simulation, phantom, and clinical results, *Appl. Opt.* 42, 135–145 (2003).
75. D. Grosenick, H. Wabnitz, K. T. Moesta, J. Mucke, P. M. Schlag, and H. Rinneberg, Time-domain scanning optical mammography: II. Optical properties and tissue parameters of 87 carcinomas, *Phys. Med. Biol.* 50, 2451–2468 (2005).
76. R. Choe, *Diffuse Optical Tomography and Spectroscopy of Breast Cancer and Fetal Brain*. PhD thesis, University of Pennsylvania, 2005.
77. A. Godavarty, M.J. Eppstein, C. Zhang, S. Theru, A. B. Thompson, M. Gurfinkel, and E. M. Sevick-Muraca, Fluorescence-enhanced optical imaging in large tissue volumes using a gain-modulated ICCD camera. *Phys. Med. Biol.* 48, 1701–1720 (2003).

## 1. Introduction

Diffuse optical tomography (DOT) is a promising new medical diagnostic [1, 2] that has been recently applied for breast cancer imaging based on endogenous tissue contrast such as hemoglobin, water and lipid [3–12]. In addition, a few breast cancer studies have used the *absorption* of exogenous molecular agents such as Indocyanine Green (ICG) to enhance tumor contrast. Evidently, leaky tumor vasculature delays ICG washout and thereby elevates its concentration in tumors relative to normal tissue [13, 14].

Fluorescent contrast agents have also been considered as a means to enhance tumor detection and characterization [15–21]. In principle, fluorescence signals can provide greater detection sensitivity and specificity compared to absorption signals, as well as access to new information about tissue micro-environment, including tissue pO<sub>2</sub>, pH, and intracellular calcium concentration [22, 23]. Indeed, the potential uses of optical fluorophores bear close resemblance to the use of contrast agents in PET and MRI [24, 25]. Successful fluorescence diffuse optical tomography (FDOT) is therefore critical for application of molecular imaging probes such as dyes [15, 17, 26–29] and molecular beacons [30] that bind to tumor-specific receptors in deep tissue.

Fluorescence tomography methods have been developed and explored in tissue phantoms [31–50], in small animals [17, 39, 51–55] and in deep tissues such as human brain [56] and

canine mammary tumors [57]. To our knowledge, however, detection and 3D *in vivo* quantification of diffuse fluorescence signals has not as yet been reported from the cancer bearing human breast.

In this paper we demonstrate *in vivo* fluorescence diffuse optical tomography (FDOT) in the human breast, reconstructing 3D tomographic maps of the tissue fluorophore distribution *in vivo*. Three cancer cases are analyzed wherein tumors exhibit fluorescence contrast up to four-fold higher than corresponding endogenous optical contrast derived using the same apparatus.

The remainder of this paper is structured as follows. The Methods section introduces the DOT instrument, describes tissue phantom and *in vivo* breast measurement protocols, and it outlines 3D fluorescence image reconstruction procedures. The Results section first establishes that the measured signal is due to ICG fluorescence rather than tissue autofluorescence and excitation light leakage. Then phantom and breast tumor observations are presented, and we demonstrate that reconstructed fluorescence from the tumor bearing breast are in good agreement with optical absorption and scattering images and with magnetic resonance imaging (MRI). In the Discussion section we summarize and compare our methods and results to related FDOT studies. We also make suggestions for improvement.

## 2. Methods

### 2.1. DOT instrument

Figure 1(a) illustrates the clinical instrument. We use it to obtain both intrinsic and fluorescent diffuse optical images of tissue phantoms and human breast. The instrument's imaging capabilities, based on endogenous contrast, have been demonstrated previously with phantoms and in human subjects [3, 4]. Furthermore, agreement with MRI in a case study of locally advanced breast cancer during neoadjuvant chemotherapy treatment has validated the potential of this DOT instrument for breast cancer imaging [4].

In practice the female subject lies in prone position with her breasts suspended in a box filled with a fluid mixture of 30% Lyposin III (Abbott Laboratories, Chicago, IL), and India ink (Black India 4415, Sanford, Bellwood, IL) whose optical properties are similar to those of human tissue. Hereafter we will refer to this mixture as "matching fluid". The cancerous breast is centered between the soft compression plate and the viewing window. The compression plate (Fig. 1(a)) contains 45 source fibers of 200  $\mu\text{m}$  in diameter (FIS) arranged in a 9 x 5 grid numbered from left to right starting with the upper left source. An optical switch (Dicon Fiber Optics, Richmond, CA) is utilized to deliver light from four sinusoidally intensity modulated (70 MHz) laser diodes operating at 650, 690, 786 and 830 nm to each grid position. The laser power level varies depending on the wavelength and the source position, with an average of 10 mW.

Light detection is accomplished in reemission through nine fibers located on the compression plate (Fig. 1(a)) and in transmission through a lens coupled 16-bit CCD (Roper Scientific, Trenton, NJ, VersArray:1300F, 1340 x 1300 pixel). The reemission fibers are connected to a frequency domain detection module which provides phase- and amplitude-data for determination of the bulk optical properties of the matching fluid and tissue. The bulk properties determined therein are used as an initial estimate in the DOT reconstruction.

For the ICG [58] fluorescence measurements (Fig. 1(b)), two spectral filters are placed in front of the CCD camera in the following order. An 830 nm bandpass filter with 10 nm FWHM (OD = 4, CVI Laser Inc.) is placed first, and a 785 nm notch filter (OD = 6, Semrock Inc) is placed second. In this way the incoming excitation light first passes through the notch filter and the possibility for detection of excitation-light-induced bandpass filter autofluorescence is eliminated.

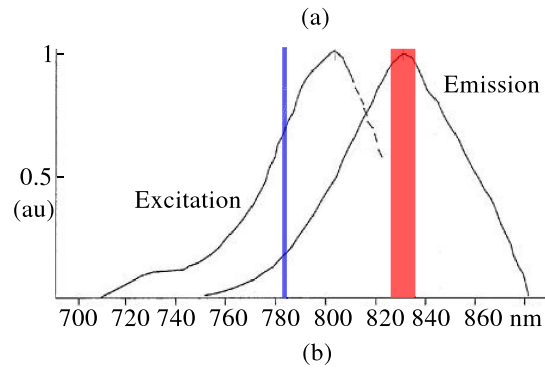
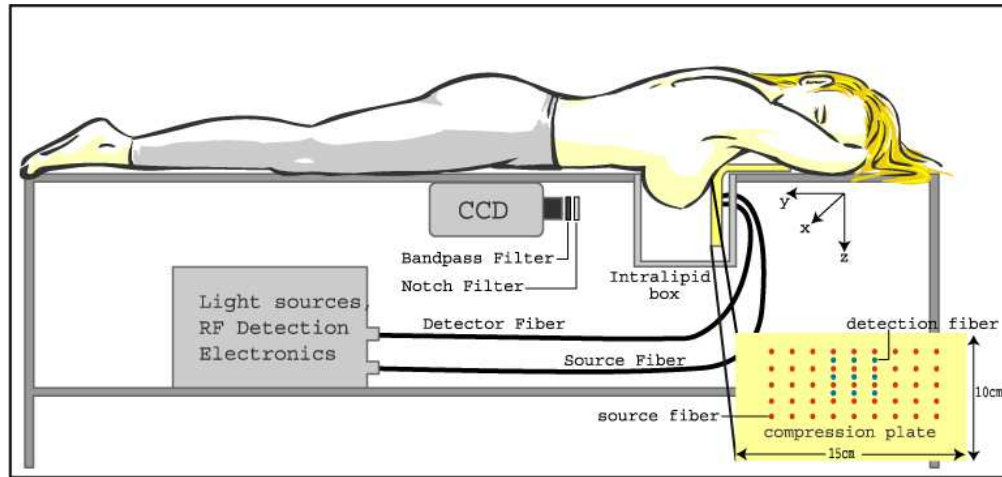


Fig. 1. Schematic of parallel plate DOT instrument. (a) The subject lies in prone position with breasts suspended in the breast box. Continuous wave (CW) transmission and frequency-domain (FD) remission measurements are performed simultaneously. Spectral filters are introduced in front of the detectors for fluorescence measurements. 45 sources and 9 FD detectors are positioned on the compression plate in a  $9 \times 5$  and  $3 \times 3$  grid arrangement. A diode laser at 786 nm is utilized for excitation of ICG and fluorescence detection (b) Excitation and emission spectra of whole blood containing 0.05 mg/ml of sterile ICG [58] are shown together with the 785 nm notch filter (blue line) and 830 nm (red shading, FWHM = 10 nm) bandpass filter.

## 2.2. Phantom measurement protocol

The clinical system has already been extensively tested for absorption and scattering contrast with tissue phantoms [3]. In the present work we report on characterization of system capability for fluorescence measurements using tissue phantoms.

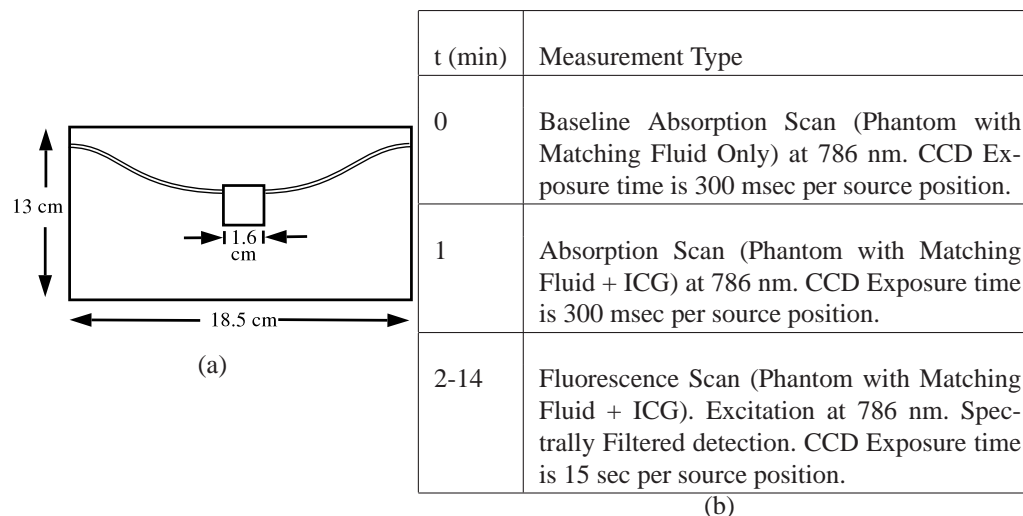


Fig. 2. (a) Illustration of the phantom (CCD view). The tube ends are attached to a pump (not shown) in order to titrate the phantom with different ICG concentrations. (b) Time-table for the phantom measurement protocol.

Figure 2 shows an illustration of the cylindrical tissue phantom with 1.6 cm length and diameter, and a wall thickness of 0.05 cm. The phantom is placed at a distance of 3 cm away from the source plate ( $y = 3$  cm) and is immersed in a matching fluid of  $\mu_a = 0.04 \text{ cm}^{-1}$  and  $\mu'_s = 8 \text{ cm}^{-1}$ . The phantom was filled with the same matching fluid via the tubes (Fig. 2(a)), and then a full scan at 786 nm was performed in order to assess phantom baseline absorption and scattering properties. The CCD camera exposure time was set to 300 msec for these measurements. The phantom was then filled with an ICG/matching-fluid mixture and another full scan at 786 nm was made at 300 msec exposure to evaluate the absorption due to ICG. Finally, a third scan was made to obtain the phantom fluorescence signal; for this scan the spectral notch and band-pass filters were attached to the CCD camera, and the exposure time was set to 15 secs. These steps were repeated for three ICG concentrations: 0.1, 1, 10  $\mu\text{M}$ .

## 2.3. In vivo measurement protocol

This prospective study was approved by the local Institutional Review Board. Informed consent form was obtained from each patient prior to imaging.

The measurements were made in three stages as outlined in the Time-table in Fig. 3: First, the intrinsic optical and physiological properties of the breast tissue were obtained from a full scan using 4 wavelengths and 45 sources positions. These measurements were conducted with the CCD camera exposure time set to 500 msec [4].

The second stage involved fluorescence measurements. To this end the spectral bandpass and notch filters were placed in front of the CCD camera, and the camera exposure time was set to 15 sec. For the fluorescence measurements it was only necessary to use one excitation wavelength, 786 nm. A monitoring scan using a single source position was conducted initially (i.e. first step of second stage) in order to derive ICG pharmacokinetics. A bolus of sterile ICG

t (min)	Measurement Type
0	Breast Endogenous Measurement. 4 Wavelengths. CCD Exposure time is 500 msec.
12	Breast ICG Pharmacokinetics Measurement. 786 nm - Spectral Filters. CCD Exposure time is 15 sec.
13	Inject ICG.
18	Breast ICG Tomographic Scan. 786 nm - Spectral Filters. CCD Exposure time is 15 sec.
30	Baseline Absorption Scan (Matching Fluid Only). 4 Wavelengths. CCD Exposure time is 500 msec.

Fig. 3. Time-table for the *in vivo* measurements.

(0.125 mg/kg, Akorn, Inc.) was given for 30 seconds, followed by a normal saline flush of 20 cc, also given for 30 seconds. The injection commenced 45 seconds after the start of the monitoring scan. After 24 frames (i.e. 6 minutes) of the monitoring scan, the full tomographic fluorescence scan was initiated. The ICG washout kinetics derived from the initial monitoring scan were used to correct for the decreasing fluorescence signal in the subsequent tomographic scan [13]. The rationale for this timing protocol is based on the concept that ICG will accumulate in the tumor due to the highly permeable tumor neo-vasculature, and that tumor ICG concentrations will remain elevated relative to those of normal breast tissue during the vascular washout phase.

In the final stage, spectral filters were removed, and a baseline transmission scan of matching fluid was conducted with the same source-detector plate separation as in the patient measurement. Baseline tomographic scans at 4 wavelengths with CCD camera exposure time set for 500 msec served as reference data in the endogenous chromophore and scattering parameter reconstruction.

#### 2.4. Data preprocessing

For each CCD camera exposure time, dark frames were recorded and subtracted from the succeeding intensity measurements. Transmission and fluorescence measurements were then digitally filtered with median ( $2 \times 2$  pixels) and Gaussian (window size = 32,  $\sigma = 6$  pixels) filters, respectively. Data binned from filtered image frames correspond to measurements at 984 detection points covering an area of  $15.6 \times 9.0$  cm.

The raw intensity plots shown in the Results section are image frames preprocessed as described above. The term *counts* in those displays denotes digitized intensity recorded by the 16-bit CCD camera.

#### 2.5. Image reconstruction algorithm

In this section, we briefly describe the tomographic methods used to obtain fluorescent contrast images. For more detail on the reconstruction techniques see references [59–62]. The present work obtains both FDOT images and tomographic (DOT) reconstructions of endogenous tissue properties such as total hemoglobin concentration (THC), blood oxygen saturation (StO<sub>2</sub>) and reduced scattering coefficient ( $\mu'_s$ ). Detailed discussion of the DOT analysis is provided in references [4, 62, 63].

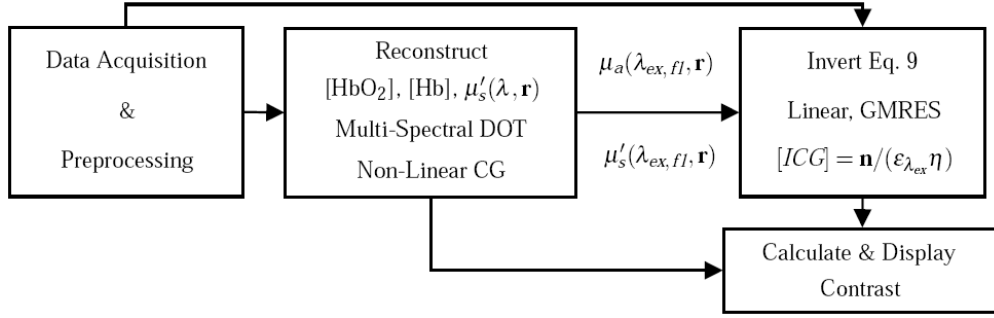


Fig. 4. Reconstruction flowchart.

Excitation and fluorescence light propagation in tissue is modeled by the diffusion equation [2,64]. This yields a set of coupled differential equations which are given below in the frequency domain:

$$-\nabla \cdot D(\lambda_{ex}, \mathbf{r}) \nabla \Phi(\lambda_{ex}, \omega, \mathbf{r}) + (\mu_a(\lambda_{ex}, \mathbf{r}) + \frac{i\omega}{v}) \Phi(\lambda_{ex}, \omega, \mathbf{r}) = q_0(\lambda_{ex}, \omega, \mathbf{r}_s), \quad (1)$$

$$-\nabla \cdot D(\lambda_{fl}, \mathbf{r}) \nabla \Phi(\lambda_{fl}, \omega, \mathbf{r}) + (\mu_a(\lambda_{fl}, \mathbf{r}) + \frac{i\omega}{v}) \Phi(\lambda_{fl}, \omega, \mathbf{r}) = \frac{n(\mathbf{r})}{1 - i\omega\tau(\mathbf{r})} \Phi(\lambda_{ex}, \omega, \mathbf{r}). \quad (2)$$

Here  $\mu_a$  denotes the light absorption due to the fluorophore and intrinsic tissue chromophores.  $\lambda_{ex(fl)}$  is the excitation (fluorescence) wavelength,  $v$  is the speed of light in the diffuse medium,  $D$  is the light diffusion coefficient given approximately in terms of the reduced scattering coefficient  $\mu'_s$  as  $1/(3\mu'_s)$  [65,66],  $\omega$  is the source modulation frequency,  $q_0(\lambda_{ex}, \omega, \mathbf{r}_s)$  is the excitation source term. Inversion of Eq. 1, using the multi-spectral data, determines  $\mu_a$ ,  $D$  as a function of position in the medium and as a function of optical wavelength. The excitation fluence rate  $\Phi(\lambda_{ex}, \omega, \mathbf{r})$  [W/m<sup>2</sup>] is computed by solving Eq. 1 using  $\mu_a(\lambda_{ex}, \mathbf{r})$ , and  $D(\lambda_{ex}, \mathbf{r})$ .  $\Phi(\lambda_{ex}, \omega, \mathbf{r})$  is the source term for Eq. 2, when multiplied by the fluorescence transfer function,  $n(\mathbf{r})/(1 - i\omega\tau(\mathbf{r}))$ ; here  $\tau(\mathbf{r})$  is the fluorescence lifetime of the fluorophore, and  $n(\mathbf{r})$  is proportional to the fluorophore concentration, i.e.,

$$n(\mathbf{r}) = [C] \times \varepsilon(\lambda_{ex}) \times \eta, \quad (3)$$

where  $[C]$  denotes the fluorophore concentration,  $\varepsilon(\lambda_{ex})$  is the extinction coefficient of the fluorophore at the excitation wavelength, and  $\eta$  is the fluorescence quantum yield.

Robin-type boundary conditions,

$$\Phi + \frac{D(\lambda)}{\alpha} \frac{d\Phi}{d\hat{\nu}} = 0, \quad (4)$$

are applied to solve Eq. 1 and 2. Here  $\alpha$  accounts for the refractive index mismatch [67] and  $\hat{\nu}$  is the outer normal vector at the measurement boundary.

Hereafter we denote the computed (measured) fluence rate with  $\Phi_{c(m)}$ . The computed fluorescence fluence rate,  $\Phi_c(\lambda_{fl}, \mathbf{r}_s, \mathbf{r}_d)$ , due to an excitation source at  $\mathbf{r}_s$  and detector at  $\mathbf{r}_d$  is derived using Eq. 2. For continuous wave (CW,  $\omega = 0$ ) measurements, the Born formulation [32] yields

$$\Phi_c(\lambda_{fl}, \mathbf{r}_s, \mathbf{r}_d) = \iint (d^3r n(\mathbf{r}) \Phi_c(\lambda_{ex}, \mathbf{r}_s, \mathbf{r}) G(\lambda_{fl}, \mathbf{r}_d, \mathbf{r})), \quad (5)$$

where  $G(\lambda_{fl}, \mathbf{r}_d, \mathbf{r})$  is the adjoint Green function [59] appropriate to Eq. 2. The measured fluorescence fluence rate  $\Phi_m(\lambda_{fl}, \mathbf{r}_s, \mathbf{r}_d)$  is then compared to  $\Theta(\mathbf{r}_s, \mathbf{r}_d, \lambda_{fl}) \Phi_c(\lambda_{fl}, \mathbf{r}_s, \mathbf{r}_d)$ . Here  $\Theta(\mathbf{r}_s, \mathbf{r}_d, \lambda_{fl})$  accounts for the unknown factors such as fiber coupling losses, light-source strengths and wavelength dependent detector quantum efficiency. A common way of reducing the detrimental effects of  $\Theta(\mathbf{r}_s, \mathbf{r}_d, \lambda)$  is to use reference data and, as suggested by Ntziachristos *et al.* [68], to normalize with the measured excitation fluence rate, i.e.,

$$\frac{\Phi_m(\lambda_{fl}, \mathbf{r}_s, \mathbf{r}_d)}{\Phi_m(\lambda_{ex}, \mathbf{r}_s, \mathbf{r}_d)} = \frac{\Theta(\mathbf{r}_s, \mathbf{r}_d, \lambda_{fl}) \Phi_c(\lambda_{fl}, \mathbf{r}_s, \mathbf{r}_d)}{\Theta(\mathbf{r}_s, \mathbf{r}_d, \lambda_{ex}) \Phi_c(\lambda_{ex}, \mathbf{r}_s, \mathbf{r}_d)}, \quad (6)$$

$$= \frac{1}{\Phi_c(\lambda_{ex}, \mathbf{r}_s, \mathbf{r}_d)} \int \left( d^3 r n(\mathbf{r}) \Phi_c(\lambda_{ex}, \mathbf{r}_s, \mathbf{r}) G(\lambda_{fl}, \mathbf{r}_d, \mathbf{r}) \right). \quad (7)$$

Here we have assumed no  $\lambda$  dependence for  $\Theta(\mathbf{r}_s, \mathbf{r}_d, \lambda)$  over the narrow range from  $\lambda_{ex}$  to  $\lambda_{fl}$ . The reconstruction volume is divided into  $N$  voxels of size  $h^3$  and the integral on the right hand side of Eq. 7 is expressed as a sum over all voxels with  $n_j = n(\mathbf{r}_j)$ :

$$\frac{\Phi_m(\lambda_{fl}, \mathbf{r}_s, \mathbf{r}_d)}{\Phi_m(\lambda_{ex}, \mathbf{r}_s, \mathbf{r}_d)} \equiv \frac{1}{\Phi_c(\lambda_{ex}, \mathbf{r}_s, \mathbf{r}_d)} \sum_{j=1}^N h^3 n_j \Phi_c(\lambda_{ex}, \mathbf{r}_s, \mathbf{r}_j) G(\lambda_{fl}, \mathbf{r}_d, \mathbf{r}_j). \quad (8)$$

We make a total of  $M$  measurements at source-detector pairs  $(r_{si}, r_{di})$ ,  $i = 1 \dots M$ , and obtain Eq. 8 for each source-detector pair. This approach translates into the matrix equality expressed below with regularization:

$$(\mathbf{J}^T \mathbf{J} + \Lambda \mathbf{L}) \mathbf{n} = \mathbf{J}^T \mathbf{y}. \quad (9)$$

Here  $\mathbf{J}$  is a  $M \times N$  matrix with the elements

$$J_{i,j} = \frac{h^3 \Phi_c(\lambda_{ex}, \mathbf{r}_{si}, \mathbf{r}_j) G(\lambda_{fl}, \mathbf{r}_{di}, \mathbf{r}_j)}{\Phi_c(\lambda_{ex}, \mathbf{r}_{si}, \mathbf{r}_{di})}, \quad (10)$$

$\mathbf{y}$  is vector of size  $M$  with  $y_i = \Phi_m(\lambda_{fl}, \mathbf{r}_{si}, \mathbf{r}_{di}) / \Phi_m(\lambda_{ex}, \mathbf{r}_{si}, \mathbf{r}_{di})$ , and  $\mathbf{n}$  is vector of size  $N$  with elements  $n_j$ .

Equation 9 uses a first-order Tikhonov prior with the regularization parameter  $\Lambda$  and a  $N \times N$  Laplacian matrix  $\mathbf{L}$ . The elements of the matrix,  $\mathbf{L}$ , are defined as  $L_{ji} = \ell$  if  $j = i$ ,  $L_{ji} = -1$  if the  $i^{th}$  voxel is a nearest neighbor of  $j^{th}$  voxel, and  $L_{ji} = 0$  otherwise [69]. Here  $\ell$  denotes the number of neighbors of  $j^{th}$  voxel. The value of the regularization parameter,  $\Lambda$ , is determined with the L-curve method [70] and typically found to be 100.

A finite element based numerical solver [71] is employed to solve the photon diffusion equation for  $\Phi_c(\lambda_{ex(fl)})$ , using absorption and scattering parameters derived from a preceding reconstruction of intrinsic optical properties. Equation 9 is then inverted using a preconditioned generalized minimal residual (GMRES) solver [69]. A typical inversion with  $M = 10000$  source-detector pairs and  $N = 40 \times 15 \times 40$  voxels takes about 40 minutes in total using an Intel<sup>(R)</sup> Xeon<sup>(TM)</sup> 3.2 GHz processor with 6 GB memory.

In this paper we present and compare the contrasts of the following parameters: THC, StO<sub>2</sub>,  $\mu'_s$  and ICG concentration. The 3D reconstruction procedure is summarized in the flowchart in Fig. 4: After the data acquisition and preprocessing step, 3D oxy- and deoxy-hemoglobin concentrations ([HbO<sub>2</sub>], [Hb]) and  $\mu'_s$  images are reconstructed iteratively using a non-linear conjugate gradient optimization routine suited to the multi-spectral method [4, 61, 62]. THC = [HbO<sub>2</sub>] + [Hb], StO<sub>2</sub> = [HbO<sub>2</sub>]/THC and  $\mu'_s$  contrast images are then obtained by scaling the image with the mean of the whole breast. As for the ICG concentration image, Eq. 9 is constructed using absorption and scattering parameters ( $\mu_a(\lambda_{ex,fl}, \mathbf{r})$ ,  $\mu'_s(\lambda_{ex,fl}, \mathbf{r})$ ) derived from

the endogenous chromophores obtained in the previous step, and inverted with a GMRES solver routine. ICG concentration is obtained from reconstructed  $\mathbf{n}$  using Eq. 3:  $[ICG] = \mathbf{n}/(\epsilon(\lambda_{ex})\eta)$ , and scaled to yield ICG contrast for *in vivo* reconstructions in a manner similar to that of endogenous contrast case. Note that  $\lambda_{ex,fl}$  corresponds to measurement wavelengths 786 and 830 nm, respectively, and  $\epsilon(\lambda_{ex}) = 254000 \text{ cm}^{-1}/\text{M}$  [72],  $\eta = 0.016$  for ICG in water [73].

The contrast image slices for all of the four parameters are displayed along with the profiles depicting the contrast along the pink lines crossing peak contrast regions. Profiles are plotted with standard deviations calculated from upper and lower pixels adjacent to the pink traces.

## 2.6. Fluorescence transillumination

In order to generate a quick but incomplete representation of fluorescence data, we also construct two-dimensional fluorescence *transillumination* images [4]. The fluorescence transillumination image is defined in terms of fluorescence and excitation fluence rate data as follows:

$$T(r_d) = -\log \left( \frac{\sum_s^{N_s} \Phi_m^{fl}(r_s, r_d)}{\sum_s^{N_s} \Phi_m^{ex}(r_s, r_d)} \right) \quad (11)$$

Here  $N_s$  refers to the number of sources used in the scan. Note that  $\Phi_m^{ex}(r_s, r_d)$  and  $\Phi_m^{fl}(r_s, r_d)$  are obtained in the first and second (full FDOT scan) stages of the *in vivo* measurement, respectively. High contrast regions in a fluorescence transillumination image indicate enhanced ICG uptake and fluorescence. Transillumination images are particularly useful for identification of surface features that have the potential to generate DOT image artifacts.

## 3. Results

### 3.1. Phantom fluorescence - raw data

We first display raw fluorescence data in order to demonstrate that light leakage is negligible. For the case of the tissue phantom we expect the fluorescence signal to emerge entirely from the small, cylindrical ICG phantom.

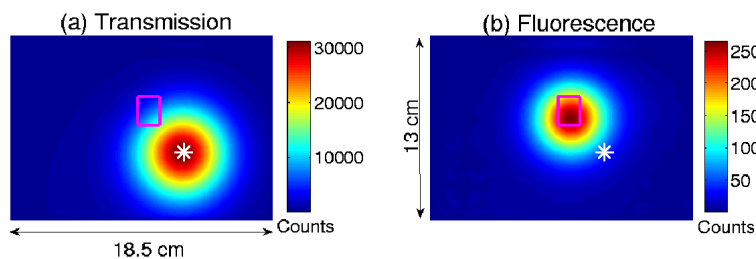


Fig. 5. Outline of the phantom is drawn in pink color and white mark (\*) shows the projection of the 43<sup>rd</sup> source location onto the detector plane. The phantom has  $1\mu\text{M}$  ICG concentration. (a) Transmission intensity at the excitation wavelength is centered at the source position. (b) Fluorescence signal originates within the object.

Figure 5 shows excitation light transmission and transmitted fluorescence intensity data from a phantom. The data were recorded with the CCD camera while the light at 786 nm was illuminating the medium from the 43<sup>rd</sup> source position. The projection of the source position on the detector plane is marked with a \*, and the target outline is drawn in pink. Notice that the excitation signal peaks very near the source position. By contrast, the fluorescence signal appears to originate within the phantom object (i.e. the object with  $1\mu\text{M}$  ICG concentration).

### 3.2. Phantom fluorescence - full 3D reconstruction

In Fig. 6, image slices from the source plane to detector plane are derived from 3D reconstructions of fluorescence (Fig. 6(a)) and absorption (Fig. 6(b)) of the phantom with [ICG] = 1  $\mu\text{M}$ . The fluorophore concentrations indicated by the color-bar of Fig. 6(a) were calibrated by titration [53]. Fluorescence and absorption results are in good agreement with respect to the phantom location. The full width at half maximum (FWHM) of the recovered images (2 cm) also approximates the size of the object (1.6 cm) reasonably well.

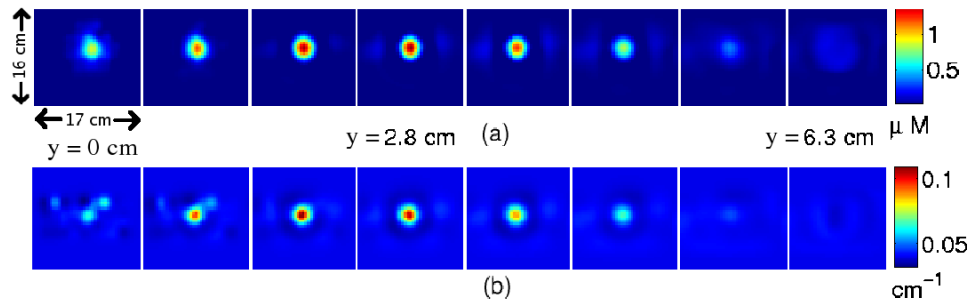


Fig. 6. Image slices from 3D reconstructions of the phantom's ICG concentration (a) and absorption at 786nm (b). Object location and size correlate well with both fluorescence and absorption images.

### 3.3. In vivo fluorescence - raw data

Similar excitation and fluorescence intensity images for *in vivo* data are displayed in Fig. 7 for two different source positions: The 23<sup>rd</sup> source in contact with tissue, and the 36<sup>th</sup> source in contact with the matching fluid. The red outline of the breast is drawn based on the photograph taken with the CCD camera. Fluorescence signal is observed to originate only from within the breast tissue.

In Fig. 8 and 9 we present fluorescence data at different time points in a patient scan (case 2) in order to demonstrate that: (1) The detected fluorescence signal is primarily due to ICG in the breast region, and (2) excitation light leakage is negligible. Figure 8 shows a plot of intensity averaged over an area of  $10 \times 10$  pixels located around the peak fluorescence signal as a function of time. This data is obtained from images acquired with 15 second exposure time while excitation light illuminates the medium from the 15<sup>th</sup> source position (marked with a white \* in Fig. 9). The green line is a simple exponential fit ( $\exp(-\beta t)$ ) to the peak fluorescence signal acquired between the time interval  $t = 3$  and  $t = 10.2$  minutes. The so-determined decay rates fall in the range reported in the literature (i.e. 0.17 - 0.21  $\text{min}^{-1}$ ) [14]. The full fluorescence scan starts at  $t = 6.6$  min with the 1<sup>st</sup> source, and at  $t = 10.2$  min the fluorescence signal is recorded from the 15<sup>th</sup> source. This data point serves as a reference to correct the full tomographic scan data for ICG washout.

Figure 9 exhibits the fluorescence intensity images from selected time points. At  $t = 0$ , before the ICG injection starts, the detected intensity represents the system noise floor (Fig. 9(a)). During the 2<sup>nd</sup> minute, when the ICG fluorescence reaches its peak, up to 3000 fluorescent CCD counts are detected (Fig. 9(b)). This count total drops to 700 as the ICG washes out from the breast at  $t = 10.2$  (min) as shown in Fig. 9(c).

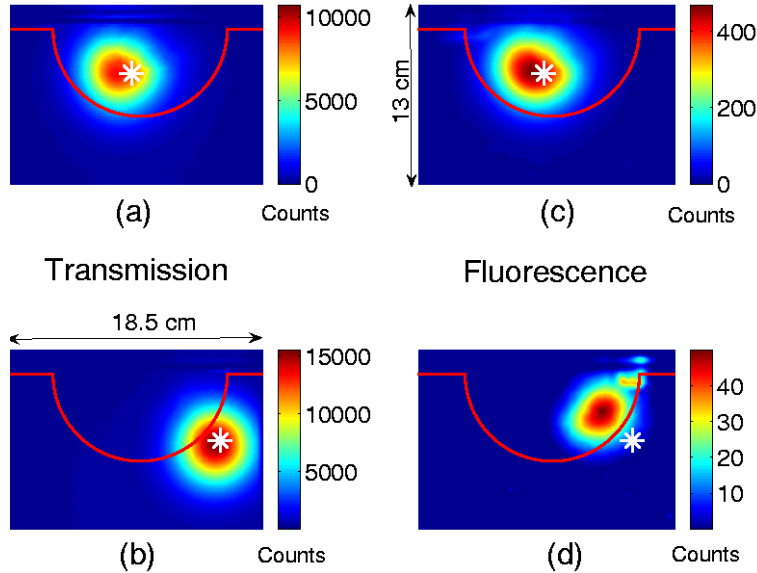


Fig. 7. The different origin of excitation transmission and fluorescence signals are demonstrated with data acquired from a patient (case 2). The breast outline is drawn with red, and the white mark (\*) shows the projection of the excitation source location onto the detector plane. Transmitted excitation light appears to come from the source position as shown in (a) and (b) for source 23 and 36, respectively. The fluorescence signal, on the other hand, is clearly contained inside the breast boundary, as demonstrated for sources 23 and 36 in (c) and (d), respectively.

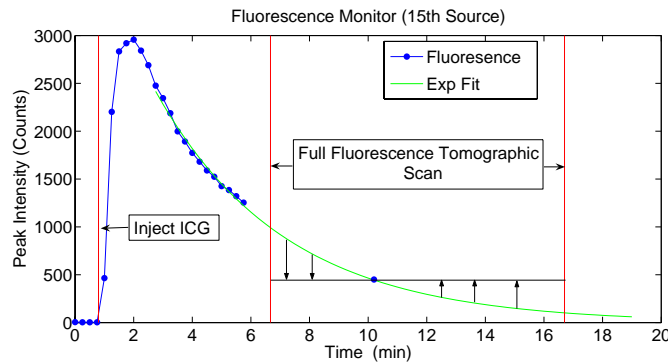


Fig. 8. Fluorescence intensity (blue line) versus time, obtained from images acquired while excitation light at 786nm illuminates the medium from the 15<sup>th</sup> source position. The green line shows the exponential fit to the fluorescence peak intensity values acquired after the 3<sup>rd</sup> minute. The full fluorescence scan starts at  $t = 6.6$  min and at  $t = 10.2$  min, fluorescence intensity is recorded with the 15<sup>th</sup> source. This data point serves as a reference to correct the full scan data.

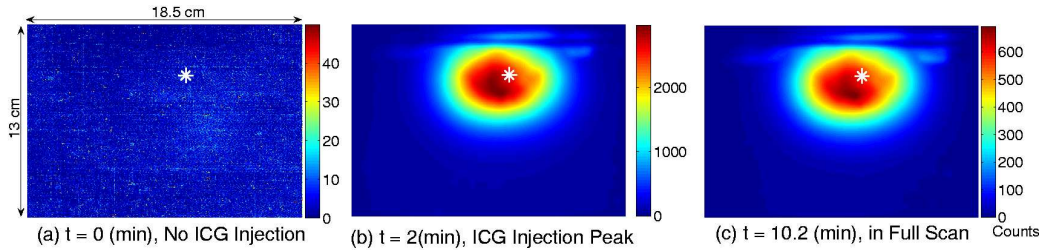


Fig. 9. Images acquired at different time points in a patient scan (case 2) while the excitation light at 786 nm illuminated the tissue from 15<sup>th</sup> source position (marked with a white \*). (a) At  $t = 0$ , before ICG injection, the detected intensity is essentially the system noise. (b)  $t = 2$  min, fluorescence signal reaches its peak. (c) At later times the signal decreases as the ICG clears out of the tissue.

### 3.4. *In vivo* fluorescence 3D reconstruction

In this section we exhibit 3D DOT contrast images of THC, StO<sub>2</sub>,  $\mu'_s(786\text{nm})$ , and ICG concentration (FDOT), 2D fluorescence transillumination, and gadolinium (Gd) enhanced MR images of the three breast cancer patients. As discussed in reference [13] both Gd and ICG can differentiate cancer based on tumor hypervascularization albeit with different mechanisms. DOT and MR studies were conducted separately with different compression schemes: axially and sagittally respectively. Here we only display sagittal views of MR images in order to show the axial depths of the tumor regions.

#### 3.4.1. Case 1

A 46-year-old pre-menopausal female diagnosed with invasive ductal carcinoma in her right breast by fine needle aspiration was recruited for the *in vivo* fluorescence DOT measurement. The palpable mass was located around 8 o'clock and was measured to be 2.5 cm in a multimodality imaging study (i.e. ultrasound, mammogram, MRI, and PET). Her breasts were almost entirely fat with average  $\mu'_s$  of  $5 \pm 2 \text{ cm}^{-1}$ . Note that the averages include the tumor region as well. The radiology report, Fig. 10(a), shows the approximate location of tumor in frontal view. Pathologic analysis found the tumor to be highly invasive with Bloom-Richardson (BR) grade of 9.

MRI sagittal slice from the right outer quadrant containing the tumor is shown in Fig. 10(b). The tumor exhibits higher intensity in the DCE-MRI image compared to the surrounding tissue, due to increased tumor vascularity and gadolinium uptake. In this slice, the tumor is located in the lower quadrant that corresponds to a plane near the detectors (i.e.  $y = 5\text{cm}$ ) in the DOT images.

Figure 10(c) displays the diffuse fluorescence transillumination image. Note that our CCD view is caudal-cranial (from foot to head), so the right and left side of Fig. 10(c) correspond to lateral and medial sides, respectively, for the right breast. Clearly a localized fluorescence uptake is observed from the transillumination image at the lateral side where the tumor is expected to be found. The enhancement seen towards the upper medial part is probably due to veins close to surface of the breast tissue, and it is in fact localized towards the detection plane in 3D reconstructions (Fig. not shown).

Figure 11(a) shows a selected slice ( $y = 5\text{cm}$ ) from the full 3D FDOT & DOT reconstructions wherein most of the parameters exhibit large contrast. This slice is near the detector plane ( $y = 6 \text{ cm}$ ). In a volume that is confirmed to be the tumor region by the Gd uptake and radiology report, the reconstructed THC,  $\mu'_s$  and ICG concentrations are higher and StO<sub>2</sub> is somewhat

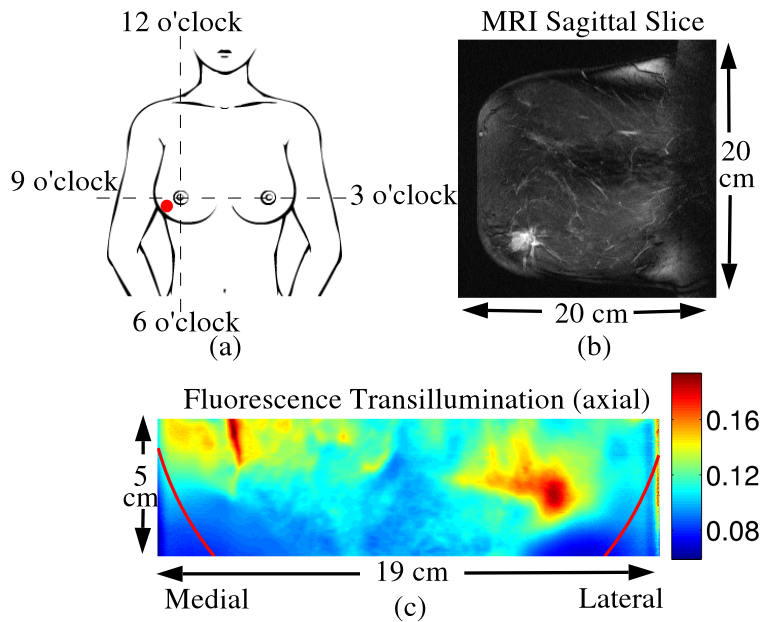


Fig. 10. (a) Illustration of the tumor location for Case 1. (b) According to the gadolinium enhanced sagittal MR image slice the tumor is located around  $y = 5$  cm position in the DOT configuration. (c) Fluorescence transillumination image obtained from patient (case 1).

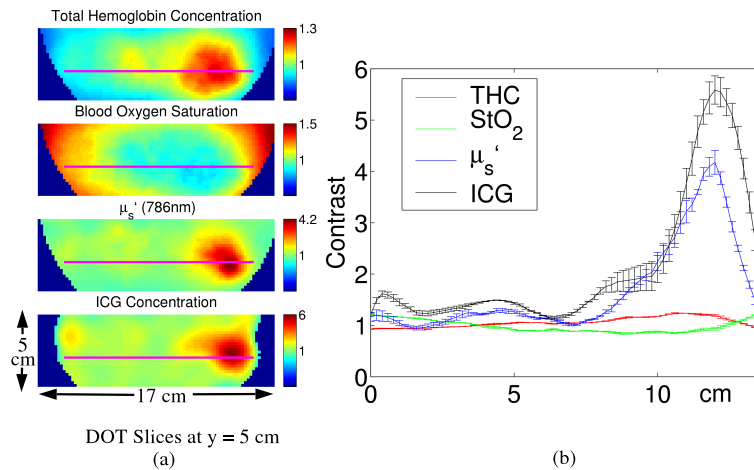


Fig. 11. Patient Case 1: Total hemoglobin concentration, blood oxygen saturation,  $\mu_s'$  (786nm) and fluorescence image slices at  $y = 5$  cm are displayed (a) with their values along a horizontal line passing through the center of tumor (b).

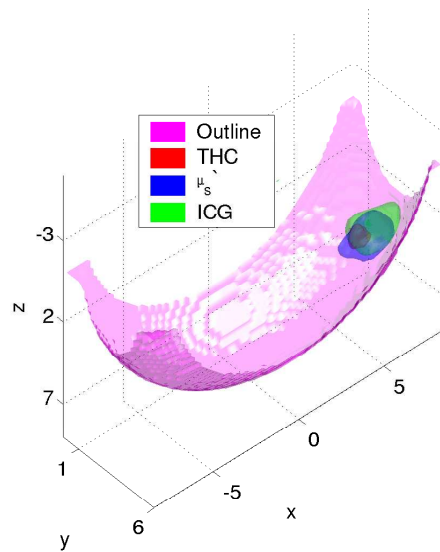


Fig. 12. Iso-surface plot of THC,  $\mu'_s(786\text{nm})$  and fluorescence at iso-values of three standard deviations above their respective means correspond to tumor location. Outline designates the border of the breast modeled as an ellipsoid using the breast photo taken with the CCD camera.

lower than the surrounding tissue. Furthermore from the profile plot in Fig. 11(b), we observe that  $\mu'_s$  and ICG concentration exhibit up to four- and 5.5-fold contrast, respectively, whereas THC contrast is only 1.3 and  $\text{StO}_2$  does not show any significant contrast.

Figure 12 shows 3D iso-surface images of THC,  $\mu'_s$  and ICG concentration contrast with iso-values set to three standard deviations above their means. The iso-surfaces of the three contrasts overlay one another quite well, and the volumetric differences may be due to real tissue physiology variation.

#### 3.4.2. Case 2

This 54-year-old pre-menopausal female was diagnosed with an invasive ductal carcinoma in her right breast by ultrasound-guided core biopsy (19 days prior to DOT). The tumor was located as an irregular lobulated hypoechoic mass of size  $1.6 \times 1.3 \times 1$  cm in the right areolar region. Figure 13(a) shows the approximate location of tumor in frontal view. Tumor BR grade was 5 according to lumpectomy.

Sagittal MR image slice in Fig. 13(b) displays the highest Gd uptake in the tumor region that would correspond to  $y = 4$  cm axial slice in the DOT configuration. The patient's breasts were heterogeneously dense and the MRI shows Gd uptake at the tumor (slightly lower than the nipple) but also diffused enhancements scattered over glandular tissue. Average  $\mu'_s$  was found to be  $7 \pm 1 \text{ cm}^{-1}$ . The fluorescence transillumination image in Fig. 13(c) shows ICG uptake distributed throughout the whole breast.

After the 3D reconstructions were carried out, contrast from the tumor region was more evident. Figure 14(a) shows the DOT contrast image slices at  $y = 4$  cm (detector plane at  $y = 6$  cm) and the corresponding profiles are plotted in Fig. 14(b). The tumor has an increase in THC and  $\mu'_s$  contrasts of 25% and 50% respectively, and it is slightly deoxygenated with decrease

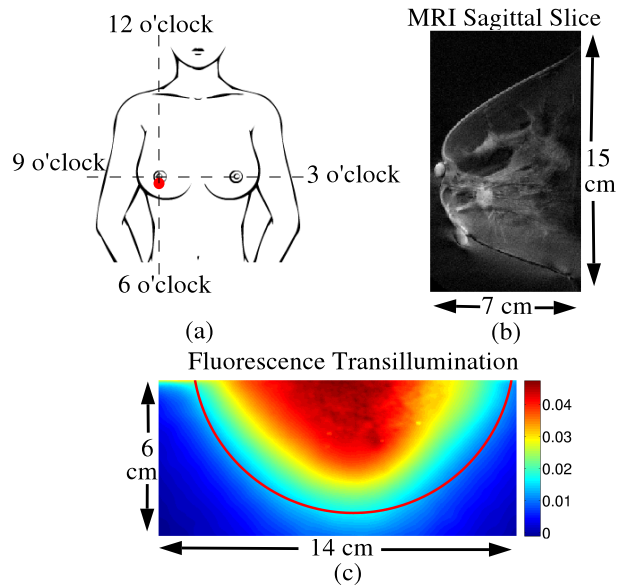


Fig. 13. (a) Illustration of the tumor location for Case 2. (b) Sagittal slice from gadolinium enhanced MR image shows a bright spot below the nipple area corresponding to the  $y = 4$  cm axial slice in the DOT configuration. (c) Fluorescence transillumination picture obtained from patient (case 2).

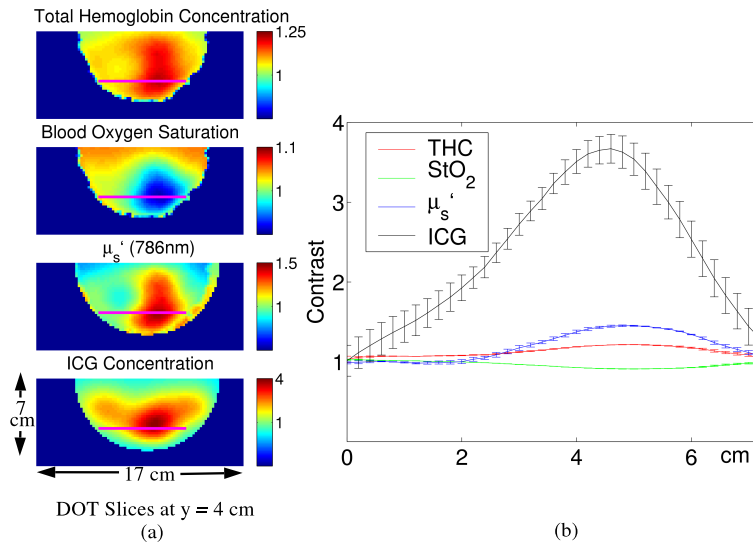


Fig. 14. Patient Case 2: Total hemoglobin concentration, blood oxygen saturation,  $\mu_s'(786\text{nm})$  and fluorescence image slices at  $y = 4$  cm are displayed (a) with their values along a horizontal line passing through the center of tumor location (b).

of 9% in  $\text{StO}_2$ . The ICG concentration provides the highest contrast of 3.5-fold. Interestingly the ICG contrast is more localized than THC and  $\mu'_s$ , potentially indicating differences between hypervascularized and leaky regions.

### 3.4.3. Case 3

The last patient case examined a 52-year-old post-menopausal female diagnosed with invasive carcinoma in her left breast by ultrasound guided core biopsy (29 days before DOT). A tumor of size 1.5 cm was located to be approximately at 7 ~ 8 o'clock retro-areolar position by a multi-imaging modality study (i.e. ultrasound, mammogram, MRI, and PET). Figure 15(a) shows the approximate location of tumor in frontal view.

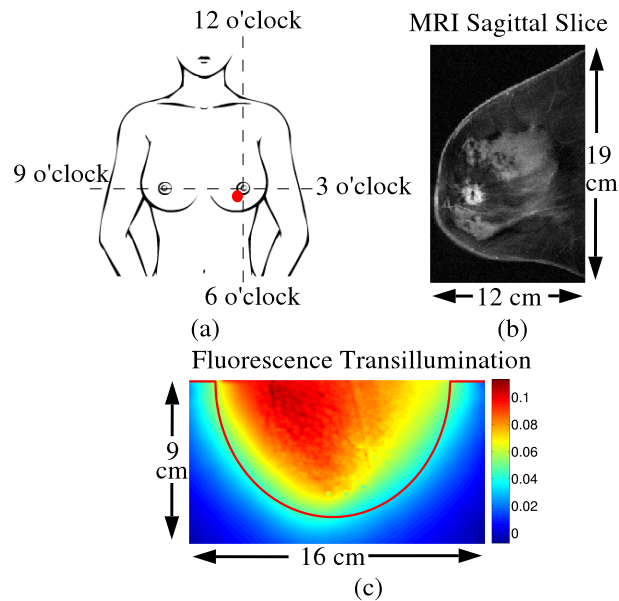


Fig. 15. (a) Illustration of the tumor location for Case 3. (b) According to the gadolinium enhanced sagittal MR image slice the tumor is located around  $y = 5$  cm position in the DOT configuration. (c) Fluorescence transillumination picture obtained from patient (case 3).

The sagittal MR image slice in Fig. 15(b) shows a localized high Gd-enhancement in the tumor region slightly below the nipple, close to the DOT detection plane. As in Case 2, this patient has heterogeneously dense breasts, and diffuse mild Gd-enhancements scattered over the glandular tissue are observed in Fig. 15(b). Average  $\mu'_s$  was found to be  $9 \pm 2 \text{ cm}^{-1}$ . In accordance with the MR image, the fluorescence transillumination image in Fig. 15(c) displays ICG fluorescence distributed throughout the whole breast.

Optical contrast tomographic image slices are shown in Fig. 16(a) at the  $y = 5$  cm slice where the parameters exhibit high contrast. The image slice corresponds to slice near the detector plane ( $y = 7$  cm). THC and  $\mu'_s$  depict contrasts of up to 1.3 and 1.5 whereas  $\text{StO}_2$  has contrast of  $-0.1$ . ICG concentration has the highest contrast of up to 4-fold. As clearly seen in Fig. 16(b) there is a difference in the locations of the contrasts volumes of the four parameters. ICG concentration and  $\text{StO}_2$  contrasts are observed to be located  $\sim 1$  cm away from THC and  $\mu'_s$  peaks which may again indicate differences in ICG uptake between hypervascularized and leaky regions.

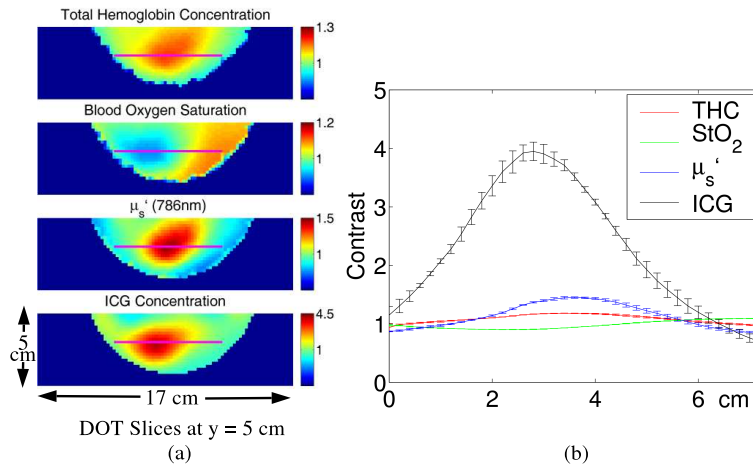


Fig. 16. Patient Case 3: Total hemoglobin concentration, blood oxygen saturation,  $\mu_s'(786\text{nm})$  and fluorescence image slices at  $y = 5$  cm are displayed (a) with their values along a horizontal line passing through the center of tumor location (b).

#### 4. Discussion

Optical imaging of biomarkers in tissue is a significant tool for enhancing cancer detection specificity and sensitivity. In this paper we have reported a feasibility study, imaging a *fluorescent* contrast agent in 3D. We clearly resolve breast cancer *in vivo*. Three patient case studies were carried out, and concurrent endogenous and exogenous images were obtained with existing DOT instrumentation.

The fluorescence imaging capabilities of our apparatus were evaluated with tumor mimicking phantom experiments. Raw data images clearly showed that the signal was due to ICG fluorescence. 3D images were reconstructed using algorithms commonly employed in DOT. Phantom scattering/absorption images as well as patient endogenous contrast images were obtained via a non-linear conjugate gradient optimization routine suited to the multi-spectral method. For fluorescence image reconstruction, on the other hand, we have essentially utilized a scheme formulated first by O'Leary *et al.* [32] for fluorescence lifetime imaging and developed further by Ntziachristos *et al.* [68]. This approach incorporates normalization of the fluorescence with excitation intensity measurements. A similar approach was also used by Patwardhan *et al.* [53]. However, in the present work the excitation intensity was measured before ICG injection, and fluence rates in Eq. 8 were calculated numerically based on the tomographically-determined heterogeneous absorption and scattering properties of the medium. Our phantom fluorescence and absorption reconstruction results suffer from the typical blurring process due to the ill-posed nature of DOT, however the FWHM of the recovered images agree well with our previous reports [3] wherein the same phantom was used for instrument characterization.

Several other FDOT schemes have been proposed. Klose and Hielscher [38] demonstrated fluorescence tomography based on radiative transport equation in 2D simulations. Their algorithm is promising for fluorescence tomography in small geometries or in media with high absorption coefficients. Eppstein *et al.* describe a 3D reconstruction algorithm [37] suited for a gain modulated intensified CCD setup. In this case background optical properties are obtained from frequency domain measurements and fluorophore (ICG) concentration is reconstructed using a Bayesian framework. The in-depth analysis presented therein incorporates measurement error and dynamic update of parameter uncertainty estimates that would potentially improve

our results.

The present paper reported endogenous contrasts along with the fluorophore concentration contrast for three patients. In all three cases the tumor region exhibited increases in THC, ICG and  $\mu'_s$  and a slight decrease in  $StO_2$ . THC,  $StO_2$  and  $\mu'_s$  contrasts of the tumor were in the 1.25 - 1.3, 0 - 0.1, and 1.5 - 4 ranges, respectively. The rise in THC is consistent with angiogenesis accompanying the tumor growth. The high oxygen demand of cancer cells might be expected to cause lower  $StO_2$ . The increase in scattering contrast can be attributed to an increase in concentration of organelles such as mitochondria due to the high metabolism in tumor cells, but might also arise (at least partially) from absorption/scattering image cross-talk. Previously we have found that spectral constraints reduce the cross-talk associated with CW data when optimum source wavelengths are used [62, 63]. The measurement wavelengths utilized in this study, however, are not quite optimum for separating absorption and scattering. Nevertheless our simulation work (results not published) has found the cross-talk to be around 30%. Therefore we believe the scattering contrast is mostly physiological, in agreement with several other researchers who have found 20% to 30% tumor scattering contrast using time-domain data [74, 75]. Overall the intrinsic contrast results presented herein agree with our previous findings [4, 76].

ICG contrast at the tumor location was visible in the fluorescence transillumination image for Case 1, but similar transillumination images for Cases 2 and 3 did not exhibit discernible contrast. In general transillumination is an insufficient radiological tool; it cannot separate the effects of light absorption and scattering within the tissue [76]. However, 3D FDOT image reconstructions based on the photon diffusion Equation provided ICG contrast images consistent with the radiology reports for all three cases. ICG concentration contrast ranged between 3.5- and 5.5-fold, possibly due to the leaky tumor vasculature.

ICG contrast in the tumor region was 3 to 4 fold higher than the THC contrast and 2 to 3 fold higher than the scattering contrast. ICG binds to blood proteins, and in the case of leaky tumor vasculature, ICG can aggregate in the tumor region while the ICG in normal tissue is washed out. Therefore, timing in the ICG fluorescence measurement plays an important role in affecting contrast, and full tomographic scans carried out during the tail of ICG temporal decay curve facilitate enhanced detection of a fluorescence signal that originates mostly from the tumor region. Thus the fluorescence contrast of the tumors is boosted.

FDOT studies for small animal imaging were applied by Graves *et al.* [51], and by Patwardhan *et al.* [53] in a similar parallel-plane source and lens coupled CCD camera system. Graves *et al.* were able to reconstruct 3D image of a fluorescent probe within a mouse tumor with submillimeter resolution. Patwardhan *et al.* studied the spatio-temporal evolution of the fluorophore distribution *in vivo*. Both studies are consistent with our work, showing preferential uptake of the target fluorescent probe in the tumor relative to normal tissue.

The purpose of this study was to investigate the feasibility of *in vivo* diffuse optical fluorescence tomography for human breast cancer. The apparatus utilized an existing breast DOT instrument with slight modifications (e.g. by coupling spectral filters). Several technical improvements can be introduced to further validate the fluorescence contrast clinically and to achieve dynamic imaging. A system that records the fluorescence and excitation signals simultaneously will provide better quantification and speed. This system can be achieved with a two-camera system or with a spectral filter wheel system coupled to the CCD camera. In a different vein, FDOT reconstruction algorithms can be improved to incorporate absorption due to ICG in the matrix inversion (see Eq. 9). One way of achieving this is to invert Eq. 9, iteratively updating ICG absorption at each step; another way would be to obtain ICG absorption directly from excitation signals in a system capable of recording fluorescence signals simultaneously. In order to accomplish dynamic imaging we need faster acquisition. To this end, we

have started to incorporate fast optical switches and gain modulated CCD intensifier units into the current system. The upgrade will provide frequency domain measurement of both the excitation and fluorescence signals thereby will allow quantification of fluorophore lifetime and superior reconstruction of absorption and scattering coefficients [77].

## 5. Conclusion

We have demonstrated three-dimensional *in vivo* DOT images of fluorescence, total hemoglobin concentration, blood oxygen saturation and scattering contrasts in three patients with tumor bearing breasts. The results were validated with phantom experiments using the same continuous wave imaging instrument.

To our knowledge, this proof of concept study is the first published report showing it is possible to detect and reconstruct breast tumor fluorescence *in vivo* in 3D with diffuse optical tomography. The large tumor contrast obtained with a non-targeted exogenous fluorophore (ICG) portends a promising future as molecularly targeted dyes and beacons become available for clinical use.

## Acknowledgments

The authors thank J. P. Culver for his initial work on this instrumentation, K. Lee, S. Konecky, D. Busch, H. Wabnitz and A. Liebert for helpful discussions, M. Grosicka-Koptyra for patient scheduling, and Y. K. Choe for illustrations. This research was supported by NIH R01-CA75124-04 and P01-CA85424. A. G. Y. acknowledges partial support from U54-CA105480 (Network for Translational Research in Optical Imaging: NTRIO).